

Large Fermi arc and robust Weyl semimetal phase in Ag_2S

Zhenwei Wang,¹ Kaifa Luo,¹ Jianzhou Zhao,^{2,3,*} and Rui Yu^{1,†}

¹*School of Physics and Technology, Wuhan University, Wuhan 430072, China*

²*Co-Innovation Center for New Energetic Materials, Southwest University of Science and Technology, Mianyang, Sichuan 621010, China*

³*Theoretical Physics and Station Q Zurich, ETH Zurich, 8093 Zurich, Switzerland*



(Received 18 September 2018; published 12 November 2019)

Three-dimensional Dirac and Weyl semimetals have attracted widespread interest in condensed matter physics and material science. Here, based on the first-principle calculations and symmetry analysis, we report that Ag_2S with $P2_12_12_1$ symmetry is a topological Dirac semimetal in the absence of spin-orbit coupling (SOC). Every Dirac point is composed of two Weyl points with the same chirality overlapping in the momentum space. After taking the SOC into consideration, each Dirac point is split into two Weyl points. The Weyl points with the opposite chirality are far from each other in the momentum space. Therefore, the Weyl pairs are not easy to annihilate and are robust in the Ag_2S compound, which also leads to long Fermi arcs on material surfaces. The robustness of the Weyl points against the strain is discussed.

DOI: [10.1103/PhysRevB.100.205117](https://doi.org/10.1103/PhysRevB.100.205117)

I. INTRODUCTION

Topological semimetals with nodal-point-type and nodal-line-type band-crossing points have attracted tremendous attention in condensed matter physics and material science [1–22]. According to the degree of degeneracy at the band-crossing point, the nodal points can be further classified as Dirac point, Weyl point, and the point beyond Dirac and Weyl types [23–26]. For example, the Dirac points are fourfold degenerate band-crossing points, which are protected by crystalline symmetries as discussed in Refs. [27–29]. The Weyl points do not need the protection of crystal symmetries except the translation invariance, while the time-reversal or spatial-inversion symmetry must be broken to guarantee their twofold degeneracy. These novel band-crossing points in practical materials lead to many exotic transport and optical properties [30–37]. An important hallmark of topological semimetals is their unusual surface states, such as the Fermi-arc states for Weyl semimetals and the drumheadlike states for nodal-line semimetals [2,3,13,14,38]. The topological nature of the Weyl points can be characterized by their topological charge. According to the no-go theorem, the Weyl points with opposite topological charge always appear in pairs in order to make the total topological charge neutral in the whole Brillouin zone (BZ) [39]. The Weyl points can only be removed if pairs of opposite Weyl points meet and annihilate each other. A large k -space separation of the Weyl nodes can guarantee a robust Weyl semimetal state, which is a prerequisite for observing the many exotic phenomena in spectroscopic and transport experiments. Therefore, it is significant to discover a more stable, nontoxic, and earth-abundant Weyl semimetal [40–47], whose Weyl nodes with opposite chirality are

separated tremendously in momentum space and locate near the chemical potential in energy.

In this work we report the Dirac and Weyl states in $P2_12_12_1$ -phase Ag_2S . By means of the first-principle calculations and symmetry analysis, we reveal that the SOC splits each Dirac point into two Weyl points with the same topological charge in Ag_2S . The formation of the Weyl points in Ag_2S is different from the Weyl points originated from the nodal-line structure. For example, in the TaAs family of materials [8,9], the bands inversion leads to 12 nodal lines in the BZ without SOC. After including the SOC effect, each nodal line is broken but leaves a pair of discrete Weyl points. The pair of Weyl points originated from the nodal line and have opposite chirality, and the distance between them is dependent on the strength of the SOC. In the TaAs compound, the distance between each positive-negative charged Weyl pair is short. Therefore, the Weyl points are easy to annihilate by perturbations and the Fermi arcs linking the Weyl points with opposite charge are short. The Weyl points in Ag_2S originated from the Dirac points. Without SOC, band inversion happens in Ag_2S and leads to four Dirac points near the Fermi energy. The Dirac points with opposite charge ± 2 , as calculated in the later section, are separated by a long distance in the momentum space. Including the SOC, each ± 2 charged Dirac point is split into two ± 1 Weyl points. While the weak SOC in Ag_2S cannot make the long separated and opposite charged Weyl points annihilate each other. Therefore, the Weyl points are robust and have long Fermi-arc states linked with them on the Ag_2S surface. The above topological properties found in $P2_12_12_1$ -phase Ag_2S are different than the topological states in the $Cmce$ -phase Ag_2S for the different symmetries of these two phases of Ag_2S . In the $Cmce$ -phase Ag_2S , a topological nodal-ring state protected by the glide symmetry of a nonsymmorphic space group appear and lead to surface drumhead states for the bulk-boundary correspondence [48].

The rest of the paper is organized as follows. In Sec. II we present the crystal structure and the first-principle calculation

*jz Zhao@swust.edu.cn

†yurui@whu.edu.cn

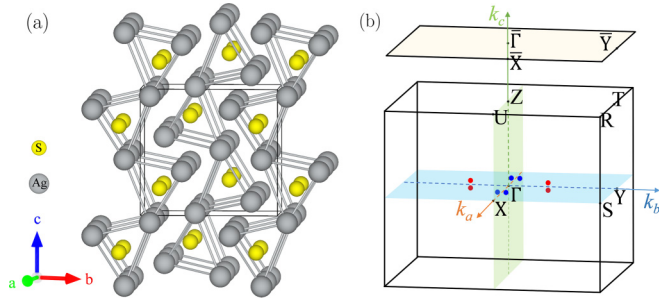


FIG. 1. (a) The crystal structure of $P2_12_12_1$ phase Ag_2S . (b) The bulk BZ and its projection onto the (001) direction. The red (blue) points indicate the positive (negative) charged Weyl points located on the $k_x = 0$ ($k_z = 0$) plane.

methodology. Without SOC, the Dirac states of Ag_2S are discussed by the first-principle calculations and the $\mathbf{k} \cdot \mathbf{p}$ model analysis in Sec. III. Then the Weyl states and the long surface Fermi-arc states with SOC are studied in Sec. IV. Discussions and conclusions are given at the end of this paper.

II. CRYSTAL STRUCTURE AND CALCULATION METHOD

The Ag_2S compound with the nonsymmorphic space group $P2_12_12_1$ (No. 19) is investigated in this work. The crystal structure is composed of chains of trigonal prisms formed by Ag atoms connected by common edges, each of these prisms being centered by an S atom as shown in Fig. 1(a). The lattice parameters and the atomic positions of Ag_2S was experimentally determined [49] and listed in Table I. The symmetry operations of the Ag_2S crystal include three screw rotations around the principal axes: $C_{2x} : (x, y, z) \rightarrow (x + \frac{1}{2}, -y + \frac{1}{2}, -z)$, $C_{2y} : (x, y, z) \rightarrow (-x, y + \frac{1}{2}, -z + \frac{1}{2})$, and $C_{2z} : (x, y, z) \rightarrow (-x + \frac{1}{2}, -y, z + \frac{1}{2})$.

The first-principle calculations are performed by using the Vienna *ab initio* simulation package (VASP) [50,51] based on the generalized gradient approximation (GGA) in the Perdew-Burke-Ernzerhof (PBE) functional and the projector augmented-wave (PAW) pseudopotential [52,53]. The energy cutoff is set to 400 eV for the plane-wave basis and BZ integration was performed on a regular mesh with $9 \times 11 \times 7$ \mathbf{k} points [54]. The band structure here is also checked by nonlocal Heyd-Scuseria-Ernzerhof (HSE06) hybrid functional calculations [55]. The surface states are studied by constructing the maximally localized Wannier functions [56–58] and using the WannierTools package [59].

TABLE I. Lattice parameters and atom positions of Ag_2S .

a (Å)	b (Å)	c (Å)	α	β	γ
6.72500	4.14790	7.29450	90	90	90
	Site	Wyckoff symbol	x	y	z
1	Ag1	4a	0.02850	0.23030	0.40790
2	Ag2	4a	0.12740	0.40740	0.82100
3	S	4a	0.22100	0.15700	0.14500

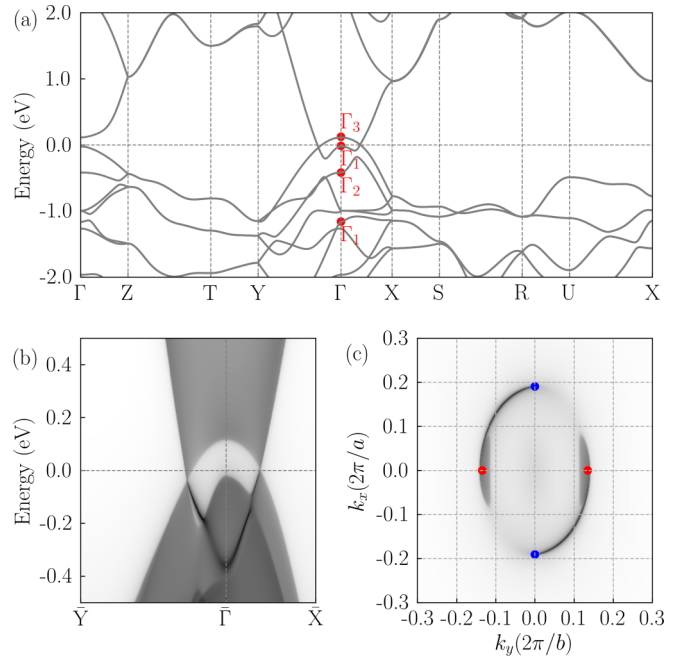


FIG. 2. (a) The band structure of $P2_12_12_1$ Ag_2S without SOC. (b) The surface states on the (001) surface. (c) The Fermi arcs connect the -2 Dirac points (blue points) and the $+2$ Dirac points (red points) on the (001) surface at the Fermi energy.

III. BAND STRUCTURE WITHOUT SOC

The electron configurations for Ag and S atoms are $[Kr]4d^{10}5s^1$ and $[Ne]3s^23p^4$, respectively. In the Ag_2S compound, the Ag atoms have a tendency to lose $5s$ electrons, while S atoms have a tendency to gain electrons from Ag atoms to form a full outer shell. One may expect an insulating phase for this compound. However, the first-principle calculations indicate that Ag_2S is a semimetal as shown in Fig. 2(a). Near the Fermi energy, the valence bands are mostly from S- $3p$ and Ag- $4d$ orbitals, while the conduction band with very strong dispersion is mostly from Ag- $5s$ states. At the Γ point, the energy of the Ag- $5s$ band is lower than the S- $3p$ and Ag- $4d$ bands about 1.1 eV, which form an energy inverted band structure. The band-crossing points in the Γ -X and Γ -Y directions are clearly shown in Fig. 2(a). These band-crossing points are protected by crystalline symmetries, which are revealed by the $\mathbf{k} \cdot \mathbf{p}$ effective model Eq. (1) near the Γ point. To construct the $\mathbf{k} \cdot \mathbf{p}$ model Hamiltonian, we find the symmetries at the Γ point include the time-reversal symmetry \hat{T} and the D_2 point group. The character table for D_2 is shown in Table II. The basis wave functions for the $\mathbf{k} \cdot \mathbf{p}$ Hamiltonian are chosen as the two energy inverted bands, the

TABLE II. Character table and basis functions for point group D_2 .

D_2	E	C_{2z}	C_{2y}	C_{2x}	Linear functions
Γ_1	+1	+1	+1	+1	–
Γ_2	+1	–1	+1	–1	y
Γ_3	+1	+1	–1	–1	z
Γ_4	+1	–1	–1	+1	x

Γ_3 and the lowest Γ_1 states as indicated in Fig. 2(a), which behave as p_z and s orbitals under the operations of the D_2 group symmetries, respectively.

The Hamiltonian, projected onto these two bases, which is invariant under all symmetry operations at Γ point, has the following form:

$$H_0(\mathbf{k}) = \begin{pmatrix} \epsilon_1 & c_1 k_x k_y + i c_2 k_z \\ \dagger & \epsilon_2 \end{pmatrix} \quad (1)$$

up to the quadratic order of \mathbf{k} , where $\epsilon_i = \epsilon_{i0} + \epsilon_{ij} k_j^2$ ($i = 1, 2$, $j = x, y, z$). The details of derivation of the $\mathbf{k} \cdot \mathbf{p}$ Hamiltonian, the parameters, and the dispersions from the $\mathbf{k} \cdot \mathbf{p}$ model compared with the first-principle results are given in Appendix A. It is easy to check that the s and p_z band are decoupled on the k_x and k_y axis, and form band-crossing points in these two axes as long as the band inversion happens between s and p_z bands. There is no band-crossing point along k_z axis for the existence of the $c_2 k_z$ term.

In the process of constructing the model Hamiltonian Eq. (1), we do not take the SOC into consideration. The spin-up and spin-down channels are decoupled. We can deal with each channels separately. Here we first consider the spin-up channel. The band-crossing points between s^* and p_z states are all twofold degenerate Weyl points. The Weyl points on the $+k_x$ axis can be rotated to the $-k_x$ direction by the C_{2z} operation. The C_{2z} rotation does not change the topological charge of the Weyl points, therefore the two Weyl points on $\pm k_x$ axis have the same topological charge. With the same argument, the two Weyl points on $\pm k_y$ axis also have the same topological charge. Because the total topological charge of the Weyl points in the BZ must be zero, the topological charge of the Weyl points on $\pm k_x$ axis must be opposite to that on the $\pm k_y$ axis. To determine the particular value of the topological charge, we can check the Berry curvature near these Weyl points. The result is that the topological charge for the Weyl points on $\pm k_x$ ($\pm k_y$) axis is negative (positive) as shown in Fig. 2(c). For the spin-down channel, there are four Weyl nodes located at the same positions in the BZ and with the same chirality as the spin-up channel Weyl nodes due to the time-reversal symmetry. One of the key characters of the Weyl semimetal is the existence of Fermi arcs on the surface of the material. To calculate the surface states, we generate the Wannier-type tight-binding Hamiltonian for Ag_2S . The calculated (001) surface states are shown in Figs. 2(b) and 2(c). It clearly shows that the Fermi arcs start from the projected points of the positive Weyl nodes and end up at the negative nodes.

IV. BAND STRUCTURE WITH SOC

In this section we consider the SOC effect on the band-crossing points discussed in the previous section. Recall the conclusions we got in the previous section that the Weyl points overlapping on the $\pm k_x$ axis have opposite chirality to the Weyl points on the $\pm k_y$ axis. The strength of the SOC cannot make the long separated opposite charged Weyl points annihilate each other. Therefore, the Dirac points are not gapped by SOC in Ag_2S but are split into two Weyl points and shifted away from the $\pm k_x$ and $\pm k_y$ axes.

The possible positions of the split Weyl points can be determined by symmetry considerations in the following way.

We denote the position of one of the Weyl points around the $+k_x$ axis as $w_1 = (k_x, k_y, k_z)$. The position of the other one Weyl point can be obtained by C_{2x} rotation, which reads $w_2 = (k_x, -k_y, -k_z)$. The remaining symmetry operators \hat{C}_{2z} , \hat{C}_{2y} , and \hat{T} transform the above two Weyl points to the $-k_x$ direction: $w_1 \xrightarrow{\hat{C}_{2z}} (-k_x, -k_y, +k_z)$, $w_2 \xrightarrow{\hat{C}_{2z}} (-k_x, +k_y, -k_z)$, $w_1 \xrightarrow{\hat{C}_{2y}} (-k_x, +k_y, -k_z)$, $w_2 \xrightarrow{\hat{C}_{2y}} (-k_x, -k_y, +k_z)$, $w_1 \xrightarrow{\hat{T}} (-k_x, -k_y, -k_z)$, $w_2 \xrightarrow{\hat{T}} (-k_x, +k_y, +k_z)$. Because there are only two Weyl points around the $-k_x$ axis, which leads to $k_z = 0$ or $k_y = 0$. Therefore, the Weyl points around $\pm k_x$ must be located on the $k_z = 0$ or $k_y = 0$ plane. With a similar argument we find that the Weyl points around the $\pm k_y$ axis are shifted to the $k_z = 0$ or $k_x = 0$ plane.

Now we construct a four-band $\mathbf{k} \cdot \mathbf{p}$ model Hamiltonian including SOC on the basis $\{s_\uparrow, p_{z\uparrow}, s_\downarrow, p_{z\downarrow}\}$, which is given as

$$H_1 = \sigma_0 \otimes H_0 + \begin{pmatrix} 0 & h_{\text{so}} \\ \dagger & 0 \end{pmatrix},$$

$$h_{\text{so}} = \begin{pmatrix} \alpha_1 k_x + i\alpha_2 k_y & \gamma_1 k_x + i\gamma_2 k_y \\ -(\gamma_1 k_x + i\gamma_2 k_y) & \beta_1 k_x + i\beta_2 k_y \end{pmatrix}, \quad (2)$$

where $\alpha_i, \beta_i, \gamma_i$ ($i = 1, 2$) are real-valued parameters depending on the strength of SOC in specific materials. h_{so} couples the orbitals with a different spin channel, leading to a full gap along the k_x and k_y axes. As the Weyl points can only be gapped by annihilation of pairs with opposite topological charges, therefore the gap closing points still exist but have been shifted away from the k_x and k_y axes. The details of this SOC included $\mathbf{k} \cdot \mathbf{p}$ model are given in Appendix B.

To check the above results, we perform the first-principle calculations with SOC. The band-crossing points on the $\pm k_{x,y}$ axes are shifted away as shown in Fig. 3(a). Carefully searching the band-crossing points in the whole BZ, we get eight Weyl points as a schematic shown in Fig. 1(b). Four Weyl points with positive chirality are located on the $k_x = 0$ plane and four with negative chirality are located on the $k_z = 0$ plane. Based on the Wannier-type tight-binding Hamiltonian, we compute the (001) surface states as shown in Figs. 3(b) and 3(c). The projections of the four negative Weyl nodes on the $k_z = 0$ plane are indicated as blue points. The positive Weyl points on the $k_x = 0$ plane overlap on the (001) surface BZ, therefore there are two red points as shown in Fig. 3(c). Two Fermi arcs start from the positive Weyl points and end in the negative Weyl points.

V. DISCUSSIONS AND CONCLUSIONS

In this section we discuss the stability of the Weyl points against strain in Ag_2S . We perform calculations for adding compressive strain on \mathbf{a} , \mathbf{b} , and \mathbf{c} directions, respectively. The results for 3% and 6% compression of each axis while retaining the lattice volume are shown in Fig. 4. For the strain adding along \mathbf{a} (\mathbf{b}) axis, the band-crossing points remaining for the lattice parameter a_0 (b_0) is compressed by 6%, but the distance between the band-crossing point on k_x and k_y directions decrease as the compressive strain increases.

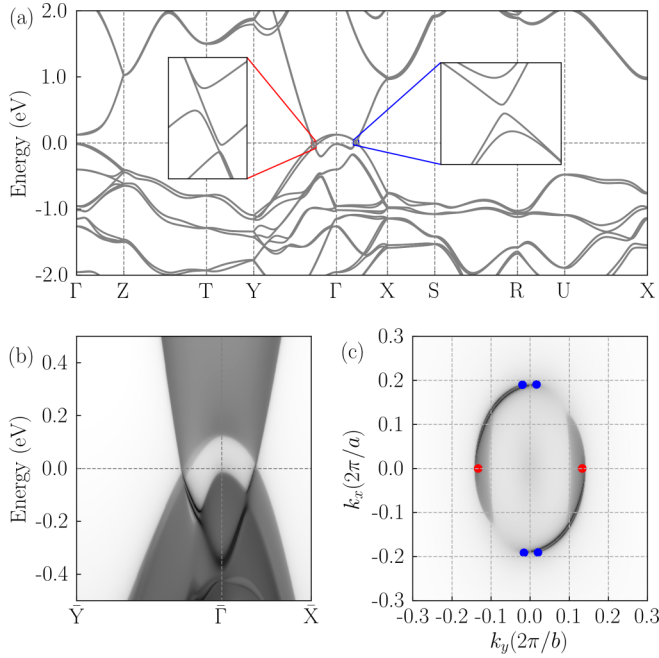


FIG. 3. (a) The band structure of Ag₂S with SOC. A gap opens around the Dirac points as shown in the inset. (b) The surface state on the (001) surface. (c) The Fermi arcs on the (001) surface with energy located at Fermi level. Each -2 charged Dirac point is split into two -1 Weyl points on the $k_z = 0$ plane (blue points), while each $+2$ charged Dirac point is split into two $+1$ Weyl points on the $k_x = 0$ plane (red points).

These results indicate that the stability of the Weyl points is weakened by compressive strain along a and b axes. For the strain effect adding along c axis, this distance increases as increasing the compressive strain. Therefore, the stability of the Weyl points is strengthened with the compressive strain along the c axis. The Weyl points in Ag₂S discussed in this work are different from the Kramers-Weyl points proposed in Ag₂Se [60–62]. Though Ag₂S and Ag₂Se possess the same symmetries, the more strong SOC in Ag₂Se annihilates the type of Weyl points of our interest existing in Ag₂S while the Kramers-Weyl points can survive and are located at the time-reversal invariant momentum points clearly presented.

In summary, based on the first-principle calculations and symmetry analysis, we predict Ag₂S can be changed from a Dirac semimetal to a Weyl semimetal by including the SOC. The Dirac points with ± 2 topological charge are protected by the crystalline symmetries and located on the k_x and k_y axes, respectively. The SOC split each Dirac point into a pair of Weyl points with the same chirality, while the strength of the SOC cannot make the opposite charged Weyl points with large distance in the momentum space meet and annihilate each other. Therefore, the Weyl points are stable in Ag₂S and lead to long Fermi arcs on the material surface.

ACKNOWLEDGMENTS

The authors thank Nan Xu for very helpful discussions. This work was supported by the National Key Research

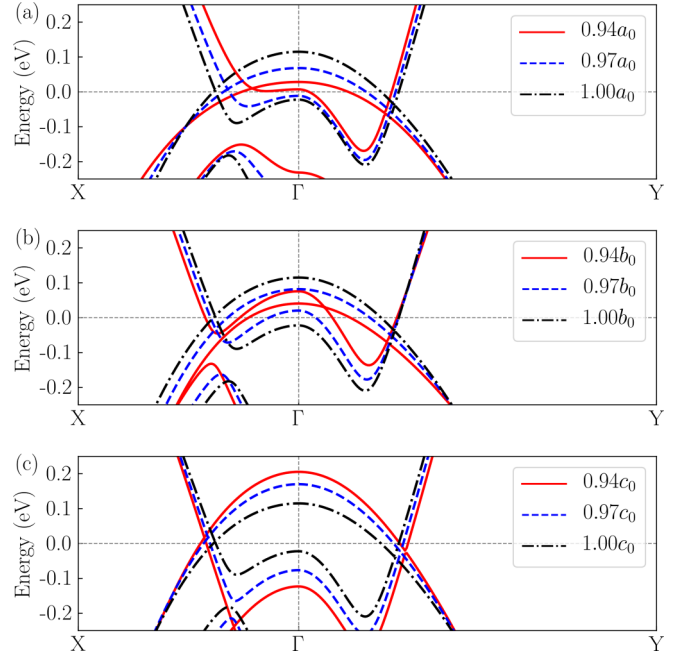


FIG. 4. The band structure of Ag₂S with a , b , and c axes compressed by 3% (blue dashed lines) and 6% (red solid lines) compared with an uncompressed lattice (black dashed-dotted lines).

and Development Program of China (No. 2017YFA0304700 and No. 2017YFA0303402), the National Natural Science Foundation of China (No. 11674077 and No. 11604273). J.Z.Z. was also supported by the Longshan academic talent research-supporting program of SWUST (17LZX527), and ETH Zurich funding for his visit. The numerical calculations in this work have been done on the supercomputing system in the Supercomputing Center of Wuhan University.

Z.W.W. and K.F.L. equally contributed to this work.

APPENDIX A: THE EFFECTIVE MODEL WITHOUT SOC

We first derive the $\mathbf{k} \cdot \mathbf{p}$ model Hamiltonian without SOC near the Γ point. According to the first-principle results, we can choose the valence state with highest energy near the Fermi energy and one state with inverted energy at the Γ point as basis functions for the $\mathbf{k} \cdot \mathbf{p}$ Hamiltonian. The irreducible representations for these states are Γ_1 and Γ_3 , respectively, in an ascending order of energy. These two bands have the symmetries the same as s and p_z orbitals, denoted $\Psi = (s, p_z)^T$.

As stated in the main text, the effective model near the Γ point is dictated by time-reversal symmetry \hat{T} and little group D_2 . The model is constructed near the Γ point, hence there is no extra phase from the fractional translation for the nonsymmorphic operations. The D_2 point group is generated by two twofold rotations C_{2z} and C_{2y} , and the symmetry operators can be represented by $C_{2y} = \tau_3$, $C_{2z} = \tau_0$, $T = \mathcal{K}$, where τ_i are Pauli matrices acting on the orbital space spanned by $\{s, p_z\}$. These symmetries give the following constraints to Hamiltonian $H(\mathbf{k})$:

$$\begin{aligned} C_{2y}H(k_x, k_y, k_z)C_{2y}^{-1} &= H(-k_x, k_y, -k_z), \\ C_{2z}H(k_x, k_y, k_z)C_{2z}^{-1} &= H(-k_x, -k_y, k_z), \\ TH(k_x, k_y, k_z)T^{-1} &= H(-k_x, -k_y, -k_z). \end{aligned} \quad (\text{A1})$$

TABLE III. Parameters for the Hamiltonian Eqs. (A2) and (B2).

ε_{10}	ε_{1x}	ε_{1y}	ε_{1z}	c_1	α_1	β_1	γ_1
-1.001	53	27	3.31	5.5	0.01	-0.2	0.18
ε_{20}	ε_{2x}	ε_{2y}	ε_{2z}	c_2	α_2	β_2	γ_2
0.106	-8.6	-3.1	0.2	1.25	-0.03	0.02	0.05

Keeping up to the quadratic order of \mathbf{k} , we find the following Hamiltonian:

$$H_0(\mathbf{k}) = \begin{pmatrix} \varepsilon_1 & c_1 k_x k_y + i c_2 k_z \\ \dagger & \varepsilon_2 \end{pmatrix} \quad (\text{A2})$$

satisfies the constraints in Eq. (A1), where

$$\varepsilon_i = \varepsilon_{i0} + \varepsilon_{ij} k_j^2 \quad (i = 1, 2, j = x, y, z) \quad (\text{A3})$$

and the c_i terms denote the lowest couplings between s and p_z orbitals. The parameters in Eq. (A2) are listed in Table III. The band dispersions from the $\mathbf{k} \cdot \mathbf{p}$ model are compared with the first-principle results as shown in Fig. 5.

APPENDIX B: THE EFFECTIVE MODEL WITH SOC

Now we deal with the coupling between spin-up and spin-down channels of s and p_z orbitals, namely, the spin-orbital coupling. The representations of symmetry operators on the chosen basis $\psi = (s_\uparrow, p_{z\uparrow}, s_\downarrow, p_{z\downarrow})^T$ are

$$C_{2y} = i\sigma_2 \otimes \tau_3, \quad C_{2z} = i\sigma_2 \otimes \tau_0, \quad T = C_{2y} \mathcal{K}. \quad (\text{B1})$$

Through the standard $\mathbf{k} \cdot \mathbf{p}$ method again, we obtain the symmetry-constrained effective Hamiltonian of SOC, up to linear order of \mathbf{k} :

$$H_{\text{so}} = \begin{pmatrix} 0 & h_{\text{so}} \\ \dagger & 0 \end{pmatrix},$$

$$h_{\text{so}} = \begin{pmatrix} \alpha_1 k_x + i\alpha_2 k_y & \gamma_1 k_x + i\gamma_2 k_y \\ -(\gamma_1 k_x + i\gamma_2 k_y) & \beta_1 k_x + i\beta_2 k_y \end{pmatrix}, \quad (\text{B2})$$

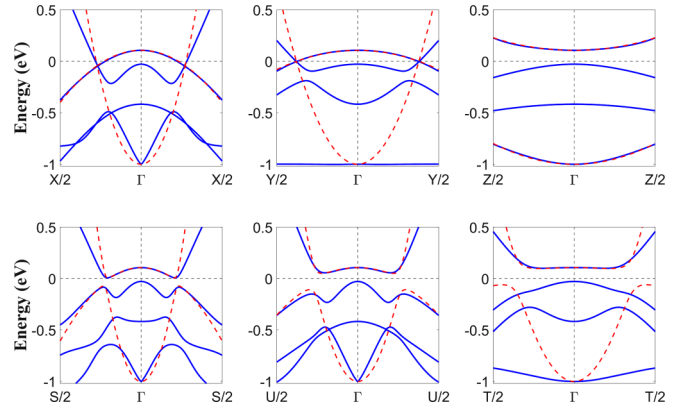


FIG. 5. The energy dispersion obtained from $\mathbf{k} \cdot \mathbf{p}$ model Hamiltonian (red dashed line) is compared with that from the first-principle calculations (blue solid line).

where σ_i are Pauli matrices acting on the spin space, and α_i, β_i , and γ_i are relevant to the coupling strengths of s_\uparrow - s_\downarrow , $p_{z\uparrow}$ - $p_{z\downarrow}$, and $s_{\uparrow(\downarrow)}$ - $p_{z\downarrow(\uparrow)}$, respectively.

At the Γ point, i.e., $k_x = k_y = k_z = 0$, these spin-up and spin-down channels are decoupled, consistent with the first-principle calculations that the s and p_z are doubly degenerate with the irreducible representation Γ_5 . The parameters in Eq. (B2) are listed in Table III. The band dispersions from the $\mathbf{k} \cdot \mathbf{p}$ model are compared with the first-principle results as shown in Fig. 6.

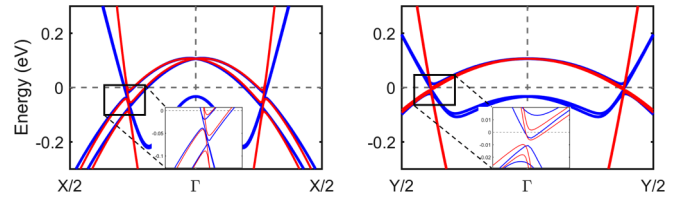


FIG. 6. The energy dispersion obtained from $\mathbf{k} \cdot \mathbf{p}$ model Hamiltonian including SOC (red solid line) is compared with that from the first-principle calculations (blue solid line).

- [1] A. A. Burkov and L. Balents, *Phys. Rev. Lett.* **107**, 127205 (2011).
- [2] X. Wan, A. M. Turner, A. Vishwanath, and S. Y. Savrasov, *Phys. Rev. B* **83**, 205101 (2011).
- [3] G. Xu, H. Weng, Z. Wang, X. Dai, and Z. Fang, *Phys. Rev. Lett.* **107**, 186806 (2011).
- [4] A. A. Burkov, M. D. Hook, and L. Balents, *Phys. Rev. B* **84**, 235126 (2011).
- [5] S. M. Young, S. Zaheer, J. C. Y. Teo, C. L. Kane, E. J. Mele, and A. M. Rappe, *Phys. Rev. Lett.* **108**, 140405 (2012).
- [6] Z. Wang, Y. Sun, X.-Q. Chen, C. Franchini, G. Xu, H. Weng, X. Dai, and Z. Fang, *Phys. Rev. B* **85**, 195320 (2012).
- [7] Z. Wang, H. Weng, Q. Wu, X. Dai, and Z. Fang, *Phys. Rev. B* **88**, 125427 (2013).
- [8] H. Weng, C. Fang, Z. Fang, B. A. Bernevig, and X. Dai, *Phys. Rev. X* **5**, 011029 (2015).
- [9] S.-M. Huang, S.-Y. Xu, I. Belopolski, C.-C. Lee, G. Chang, B. Wang, N. Alidoust, G. Bian, M. Neupane, C. Zhang *et al.*, *Nat. Commun.* **6**, 7373 (2015).
- [10] S. Borisenko, Q. Gibson, D. Evtushinsky, V. Zabolotnyy, B. Büchner, and R. J. Cava, *Phys. Rev. Lett.* **113**, 027603 (2014).
- [11] B. Q. Lv, H. M. Weng, B. B. Fu, X. P. Wang, H. Miao, J. Ma, P. Richard, X. C. Huang, L. X. Zhao, G. F. Chen, Z. Fang, X. Dai, T. Qian, and H. Ding, *Phys. Rev. X* **5**, 031013 (2015).
- [12] J. Zhao, R. Yu, H. Weng, and Z. Fang, *Phys. Rev. B* **94**, 195104 (2016).
- [13] H. Weng, Y. Liang, Q. Xu, R. Yu, Z. Fang, X. Dai, and Y. Kawazoe, *Phys. Rev. B* **92**, 045108 (2015).
- [14] R. Yu, H. Weng, Z. Fang, X. Dai, and X. Hu, *Phys. Rev. Lett.* **115**, 036807 (2015).
- [15] A. A. Soluyanov, D. Gresch, Z. Wang, Q. Wu, M. Troyer, X. Dai, and B. A. Bernevig, *Nature (London)* **527**, 495 (2015).
- [16] Y. Sun, S.-C. Wu, M. N. Ali, C. Felser, and B. Yan, *Phys. Rev. B* **92**, 161107(R) (2015).

- [17] J. Ruan, S.-K. Jian, H. Yao, H. Zhang, S.-C. Zhang, and D. Xing, *Nat. Commun.* **7**, 11136 (2016).
- [18] J. Ruan, S.-K. Jian, D. Zhang, H. Yao, H. Zhang, S.-C. Zhang, and D. Xing, *Phys. Rev. Lett.* **116**, 226801 (2016).
- [19] T. Bzdušek, Q. Wu, A. Rüegg, M. Sigrist, and A. A. Soluyanov, *Nature (London)* **538**, 75 (2016).
- [20] H. Weng, X. Dai, and Z. Fang, *J. Phys. Condens. Matter* **28**, 303001 (2016).
- [21] S.-S. Wang, Y. Liu, Z.-M. Yu, X.-L. Sheng, and S. A. Yang, *Nat. Commun.* **8**, 1844 (2017).
- [22] N. P. Armitage, E. J. Mele, and A. Vishwanath, *Rev. Mod. Phys.* **90**, 015001 (2018).
- [23] H. Weng, C. Fang, Z. Fang, and X. Dai, *Phys. Rev. B* **94**, 165201 (2016).
- [24] J. Wang, X. Sui, W. Shi, J. Pan, S. Zhang, F. Liu, S.-H. Wei, Q. Yan, and B. Huang, *Phys. Rev. Lett.* **119**, 256402 (2017).
- [25] B. Bradlyn, J. Cano, Z. Wang, M. G. Vergniory, C. Felser, R. J. Cava, and B. A. Bernevig, *Science* **353**, aaf5037 (2016).
- [26] Z. Zhu, G. W. Winkler, Q. Wu, J. Li, and A. A. Soluyanov, *Phys. Rev. X* **6**, 031003 (2016).
- [27] B.-J. Yang and N. Nagaosa, *Nat. Commun.* **5**, 4898 (2014).
- [28] Q. D. Gibson, L. M. Schoop, L. Muechler, L. S. Xie, M. Hirschberger, N. P. Ong, R. Car, and R. J. Cava, *Phys. Rev. B* **91**, 205128 (2015).
- [29] P. Tang, Q. Zhou, G. Xu, and S.-C. Zhang, *Nat. Phys.* **12**, 1100 (2016).
- [30] P. Hosur and X. Qi, *C. R. Phys.* **14**, 857 (2013).
- [31] H. Wei, S.-P. Chao, and V. Aji, *Phys. Rev. Lett.* **109**, 196403 (2012).
- [32] D. T. Son and B. Z. Spivak, *Phys. Rev. B* **88**, 104412 (2013).
- [33] C.-X. Liu, P. Ye, and X.-L. Qi, *Phys. Rev. B* **87**, 235306 (2013).
- [34] P. E. C. Ashby and J. P. Carbotte, *Phys. Rev. B* **87**, 245131 (2013).
- [35] S.-Y. Xu, I. Belopolski, N. Alidoust, M. Neupane, G. Bian, C. Zhang, R. Sankar, G. Chang, Z. Yuan, C.-C. Lee, S.-M. Huang, H. Zheng, J. Ma, D. S. Sanchez, B. Wang, A. Bansil, F. Chou, P. P. Shibayev, H. Lin, S. Jia, and M. Z. Hasan, *Science* **349**, 613 (2015).
- [36] J. Xiong, S. K. Kushwaha, T. Liang, J. W. Krizan, M. Hirschberger, W. Wang, R. J. Cava, and N. P. Ong, *Science* **350**, 413 (2015).
- [37] X. Huang, L. Zhao, Y. Long, P. Wang, D. Chen, Z. Yang, H. Liang, M. Xue, H. Weng, Z. Fang, X. Dai, and G. Chen, *Phys. Rev. X* **5**, 031023 (2015).
- [38] A. M. Essin and V. Gurarie, *Phys. Rev. B* **84**, 125132 (2011).
- [39] H. B. Nielsen and M. Ninomiya, *Phys. Lett. B* **130**, 389 (1983).
- [40] G. Chang, S.-Y. Xu, D. S. Sanchez, S.-M. Huang, C.-C. Lee, T.-R. Chang, G. Bian, H. Zheng, I. Belopolski, N. Alidoust *et al.*, *Sci. Adv.* **2**, e1600295 (2016).
- [41] F. Y. Bruno, A. Tamai, Q. Wu, I. Cucchi, C. Barreateau, A. De La Torre, S. McKeaun Walker, S. Riccò, Z. Wang, T. K. Kim *et al.*, *Phys. Rev. B* **94**, 121112(R) (2016).
- [42] G. Autès, D. Gresch, M. Troyer, A. A. Soluyanov, and O. V. Yazyev, *Phys. Rev. Lett.* **117**, 066402 (2016).
- [43] D. Takane, Z. Wang, S. Souma, K. Nakayama, T. Nakamura, H. Oinuma, Y. Nakata, H. Iwasawa, C. Cacho, T. Kim, K. Horiba, H. Kumigashira, T. Takahashi, Y. Ando, and T. Sato, *Phys. Rev. Lett.* **122**, 076402 (2019).
- [44] M. Breitzkreuz and P. W. Brouwer, *Phys. Rev. Lett.* **123**, 066804 (2019).
- [45] G. Chang, J. Yin, T. Neupert, D. S. Sanchez, I. Belopolski, S. S. Zhang, T. A. Cochran, M.-C. Hsu, S.-M. Huang, B. Lian, S.-Y. Xu, H. Lin, and M. Z. Hasan, *arXiv:1906.03207*.
- [46] N. B. M. Schroter, D. Pei, M. G. Vergniory, Y. Sun, K. Manna, F. de Juan, J. A. Krieger, V. Süss, M. Schmidt, P. Dudin, B. Bradlyn, T. K. Kim, T. Schmitt, C. Cacho, C. Felser, V. N. Strocov, and Y. Chen, *Nat. Phys.* **15**, 759 (2019).
- [47] Z. Rao, H. Li, T. Zhang, S. Tian, C. Li, B. Fu, C. Tang, L. Wang, Z. Li, W. Fan, J. Li, Y. Huang, Z. Liu, Y. Long, C. Fang, H. Weng, Y. Shi, H. Lei, Y. Sun, T. Qian, and H. Ding, *Nature (London)* **567**, 496 (2019).
- [48] H. Huang, K.-H. Jin, and F. Liu, *Phys. Rev. B* **96**, 115106 (2017).
- [49] D. Santamaría-Pérez, M. Marqués, R. Chulía-Jordán, J. M. Menendez, O. Gomis, J. Ruiz-Fuertes, J. A. Sans, D. Errandonea, and J. M. Recio, *Inorg. Chem.* **51**, 5289 (2012).
- [50] G. Kresse and J. Furthmüller, *Comput. Mater. Sci.* **6**, 15 (1996).
- [51] G. Kresse and J. Furthmüller, *Phys. Rev. B* **54**, 11169 (1996).
- [52] P. E. Blöchl, *Phys. Rev. B* **50**, 17953 (1994).
- [53] J. P. Perdew, K. Burke, and M. Ernzerhof, *Phys. Rev. Lett.* **77**, 3865 (1996).
- [54] H. J. Monkhorst and J. D. Pack, *Phys. Rev. B* **13**, 5188 (1976).
- [55] J. Heyd, G. E. Scuseria, and M. Ernzerhof, *J. Chem. Phys.* **118**, 8207 (2003).
- [56] N. Marzari and D. Vanderbilt, *Phys. Rev. B* **56**, 12847 (1997).
- [57] I. Souza, N. Marzari, and D. Vanderbilt, *Phys. Rev. B* **65**, 035109 (2001).
- [58] N. Marzari, A. A. Mostofi, J. R. Yates, I. Souza, and D. Vanderbilt, *Rev. Mod. Phys.* **84**, 1419 (2012).
- [59] Q. Wu, S. Zhang, H.-F. Song, M. Troyer, and A. A. Soluyanov, *Comput. Phys. Commun.* **224**, 405 (2018).
- [60] C.-L. Zhang, F. Schindler, H. Liu, T.-R. Chang, S.-Y. Xu, G. Chang, W. Hua, H. Jiang, Z. Yuan, J. Sun, H.-T. Jeng, H.-Z. Lu, H. Lin, M. Z. Hasan, X. C. Xie, T. Neupert, and S. Jia, *Phys. Rev. B* **96**, 165148 (2017).
- [61] B. Wan, F. Schindler, K. Wang, K. Wu, X. Wan, T. Neupert, and H.-Z. Lu, *J. Phys.: Condens. Matter* **30**, 505501 (2018).
- [62] G. Chang, B. J. Wieder, F. Schindler, D. S. Sanchez, I. Belopolski, S.-M. Huang, B. Singh, D. Wu, T.-R. Chang, T. Neupert, S.-Y. Xu, H. Lin, and M. Z. Hasan, *Nat. Mater* **17**, 978 (2018).